Supporting Information

Solvent-Dependent Self-Assembly of N-Annulated Perylene Diimides. From Dimers to Supramolecular Polymers

Cristina Naranjo,[a] Azahara Doncel-Giménez,[b] Rafael Gómez,[a] Juan Aragó,[b*] Enrique Ortí,[b*] and Luis Sánchez[a*]

[a] *Departamento de Química Orgánica, Facultad de Ciencias Químicas, Universidad Complutense de Madrid, E-28040 Madrid, Spain.*

[b] *Instituto de Ciencia Molecular (ICMol), Universidad de Valencia, c/Catedrático José Beltrán, 2, E-46980 Paterna, Spain.*

Contents:

1. Experimental section

General. All solvents were dried according to standard procedures. Reagents were used as purchased. All air-sensitive reactions were carried out under argon atmosphere. Flash chromatography was performed using silica gel (Merck, Kieselgel 60, 230-240 mesh or Scharlau 60, 230-240 mesh). Analytical thin-layer chromatography (TLC) was performed using aluminium-coated Merck Kieselgel 60 F254 plates. NMR spectra were recorded on a Bruker Avance 300 MHz (^{1}H: 300 MHz; ^{13}C: 75 MHz) spectrometer at 25 ºC using partially deuterated solvents as internal standards. Coupling constants (J) are denoted in Hz and chemical shifts (δ) in ppm. Multiplicities are denoted as follows: s = singlet, d = doublet, t = triplet, q = quartet, quin = quintuplet, m = multiplet, br = broad. FTIR spectra were recorded on a Bruker Tensor 27 (ATR device) spectrometer. FTIR spectra in film were recorded on a Jasco FT-IR4600 spectrometer using a CaF_2 cell with a path length of 0.1 nm. UV-Vis spectra were registered on a Jasco-V630 spectrophotometer equipped with a Peltier thermoelectric temperature controller. All the heating and cooling cycles were performed at 1 ºC·min^{-1}. The freshly prepared solutions were measured and, after that, the samples were heated up to 90 ºC. The samples at 90 ºC were registered and cooled to 10 ºC. Emission spectra were recorded on a Perkin-Elmer LS55 spectrophotometer. Atomic force microscopy (AFM) images were taken on a SPM Nanoscope IIIa multimode microscope working on tapping mode with a TESPSS tip (Veeco) at a working frequency of ~235 kHz. High-resolution mass spectra (HRMS) were recorded on a MALDI Bruker daltonics Ultraflex TOF/TOF spectrometer.

2. Synthetic details and characterization
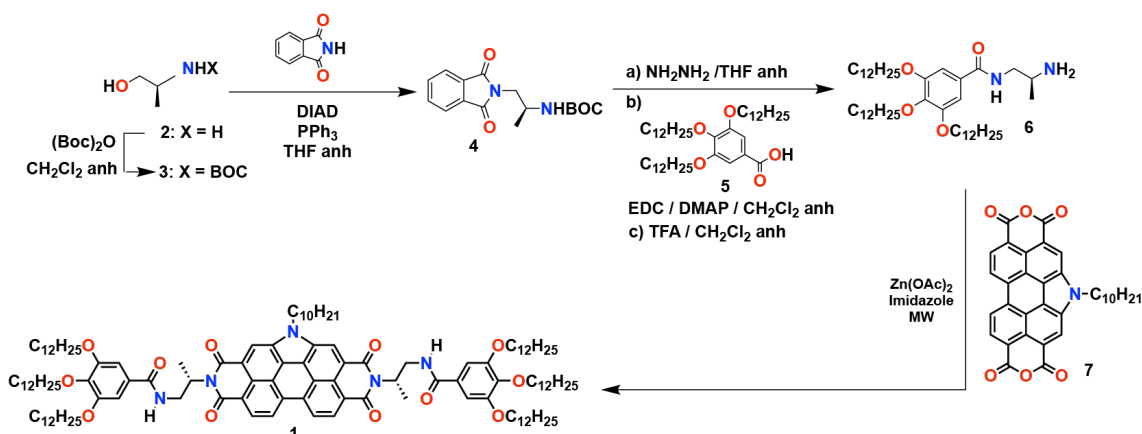
Scheme S1. Synthesis of the reported N-annulated PBI **1**.

Compounds **2-7**[S1,S2] were prepared according to previously reported synthetic procedures and showed identical spectroscopic properties to those reported therein.

N-N-((2S,2S)-(5-decyl-1,3,7,9-tetraoxo-1,5,7,9-tetrahydro-2H-pyrido[3',4',5':4,5]naphto[2,1,8-cde]pyrido[3',4',5':4,5]naphtha[8,1,2-ghi]isoindole-2,8(3H)-dyil)bis(propone-2,1-dyil))bis(3,4,5-tris(dodecyloxy)benzamide) (1)
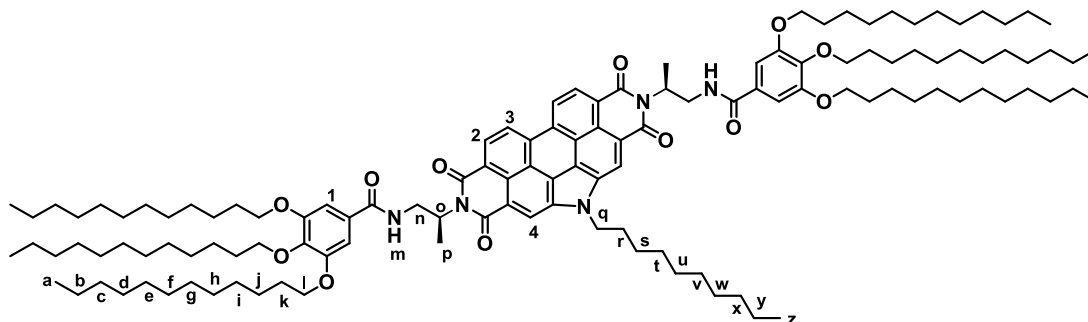

Compound **7** (50 mg, 0.09 mmol), amine **6** (147.42 mg, 0.20 mmol), zinc acetate (16.8 mg, 0.09 mmol), and imidazole (650 mg) were introduced in a 10 mL microwave tube. After three cycles argon/vacuum, the compound mixture was reacted in a microwave (165 ºC, 35 min). The crude was redissolved in CH_2Cl_2 and washed with brine. Organic layers were dried over $MgSO_4$ and the solvent was evaporated under reduced pressure. The residue was purified by column chromatography (CH_2Cl_2/MeOH 10/0.1). Compound **1** was obtained as a bright red solid: 42 %. ^1H NMR (700 MHz, THF-d8, 328 K) δ (ppm): 8.71 (s, 2H, H_m), 8.31 (br, 2H, H_4), 8.22 (br, 2H, H_3), 8.13 (br, 2H, H_2), 7.29 (s, 4H, H_1), 5.82 (br, 2H, H_q), 4.75 (br, 2H, H_o), 4.44 (br, 2H, H_n), 4.06 (br, 2H, H_n), 3.88 (m, 12H, H_l), 1.95 (m, 2H, H_r), 1.63 (m, 12H, H_k), 1.42 (m, 6H, H_p), 1.35–1.12 (m, 122H, H_{b-j} and H_{s-y}), 0.86 (m, 21H, H_a). FTIR (cm⁻¹): 743, 759, 805, 842, 899, 1021, 1064, 1113, 1179, 1223, 1259, 1304, 1334, 1377, 1423, 1464, 1494, 1539, 1556, 1580, 1601, 1644, 1689,

2852, 2921, 3351. HR-MS-MALDI-TOF m/z: calculated: $C_{126}H_{195}N_5O_{12}$ [M+2]$^+$ 1972.4802, found: 1972.4650.

3. Collection of spectra

^{1}H NMR (THF-d8, 700 MHz, 328 K) of compound **1**.
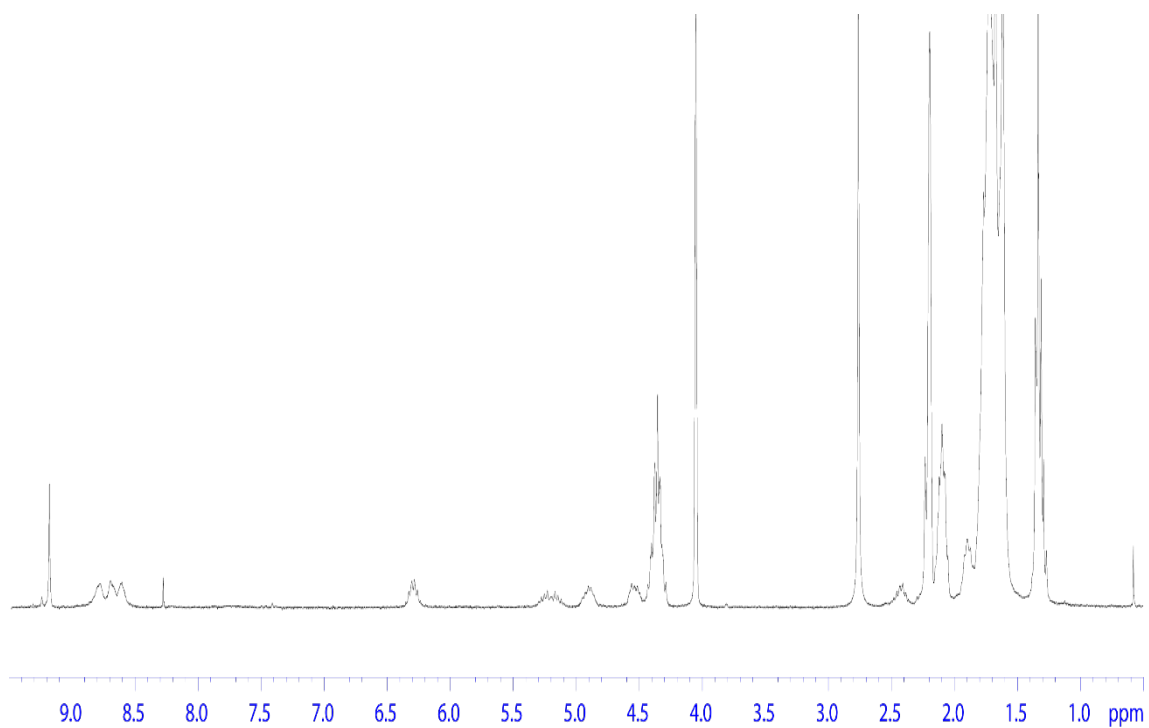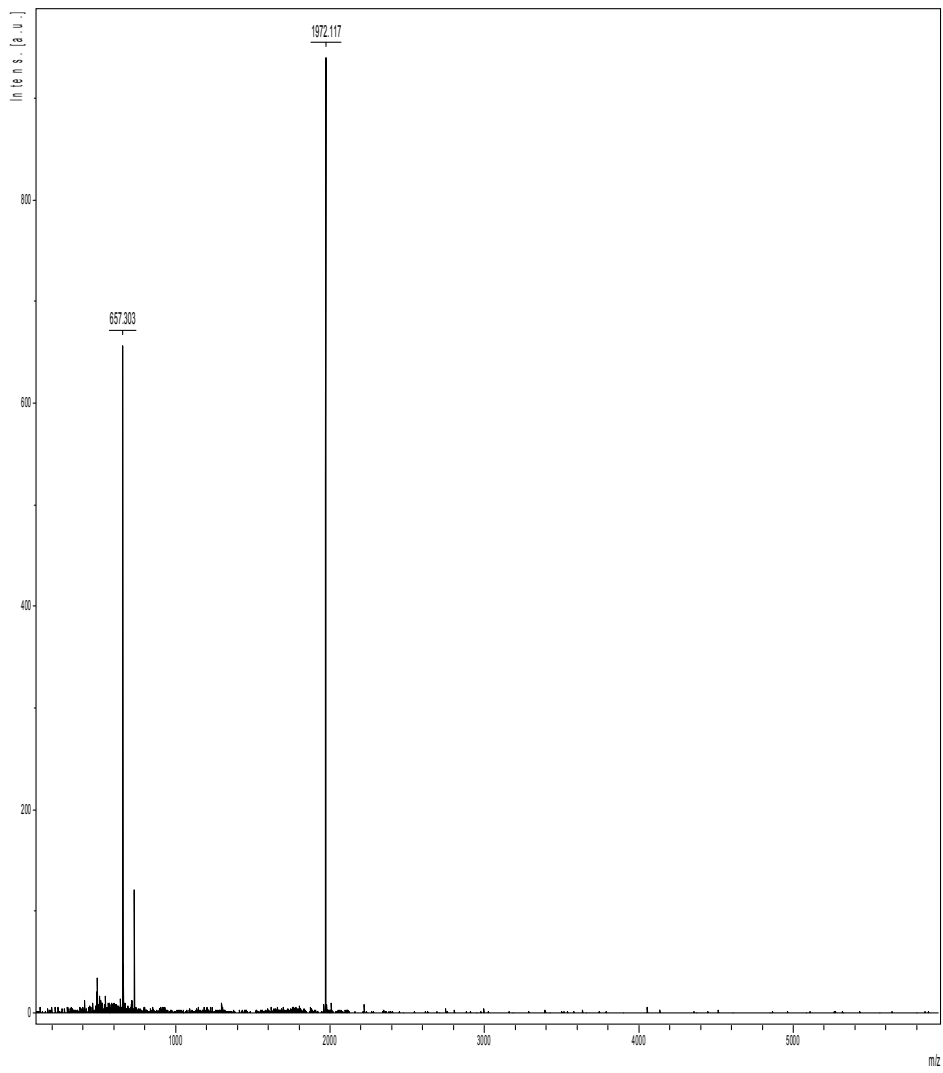
4. Supplementary Figures and Tables

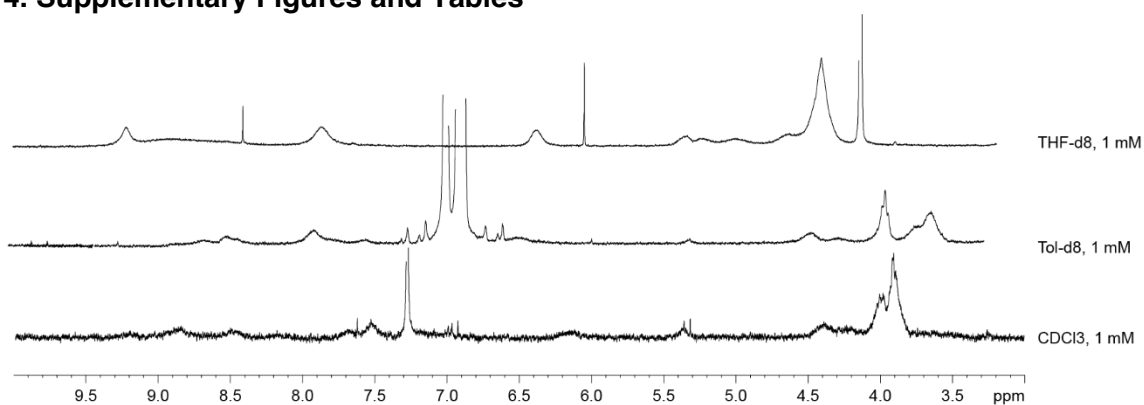**Figure S1**. Partial ^{1}H NMR spectra of **1** recorded in different solvents showing the aromatic and some of the aliphatic protons (300 MHz, 298 K).
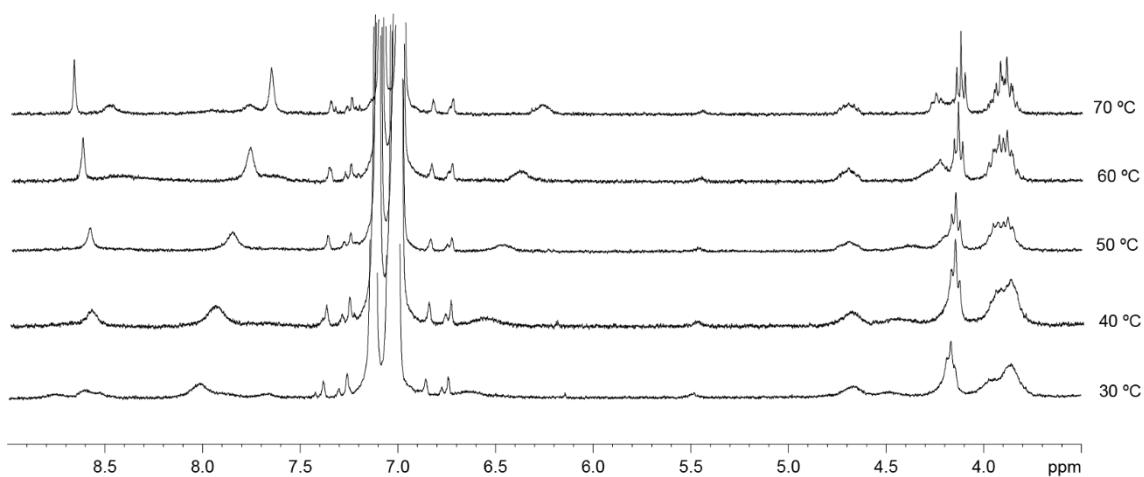

Figure S2. Partial ^{1}H NMR spectra of **1** recorded at different temperatures showing the aromatic and some of the aliphatic protons (Tol-d8; 300 MHz).
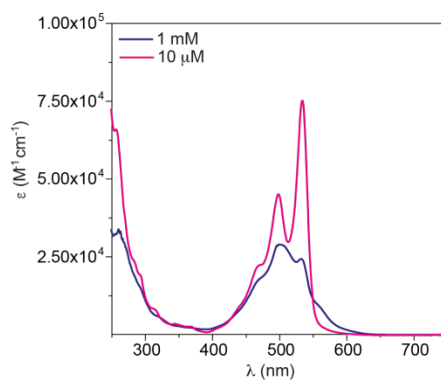

Figure S3. UV-Vis spectra of **1** in CHCl$_3$ at c_T = 1 mM and 10 µM at 20 °C.
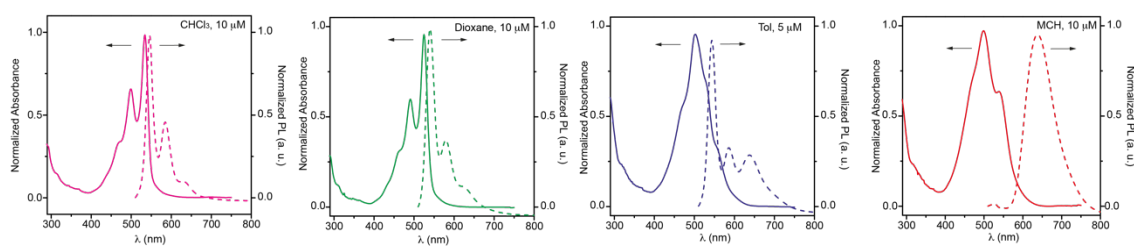
Figure S4. UV-Vis (solid line) and emission (dashed line) spectra of **1** in different solvents (20 °C; λ_{exc} = 505 nm).

1a: ΔE = 13.11 kJ/mol   **1b:** ΔE = 11.59 kJ/mol   **1c:** ΔE = 19.07 kJ/mol

1d: ΔE = 0.00 kJ/mol   **1e:** ΔE = 0.46 kJ/mol

1f: ΔE = 55.05 kJ/mol   **1g:** ΔE = 24.21 kJ/mol

1.85 Å   1.89 Å   1.90 Å

Figure S5. Minimum-energy structures (with their relative energy indicated) computed at the GFN2-xTB level in CHCl₃ for the most stable conformers of monomer **1**. Side and top views of conformers **1f** and **1g** are provided to show the formation of seven membered H-bonded pseudocycles.

1d: ΔE = 0.00 kJ/mol

2.93 Å   3.02 Å

1e: ΔE = 21.00 kJ/mol

2.94 Å

3.11 Å

1f: ΔE = 55.05 kJ/mol

1.87 Å

1g: ΔE = 24.21 kJ/mol

1.88 Å

1.92 Å

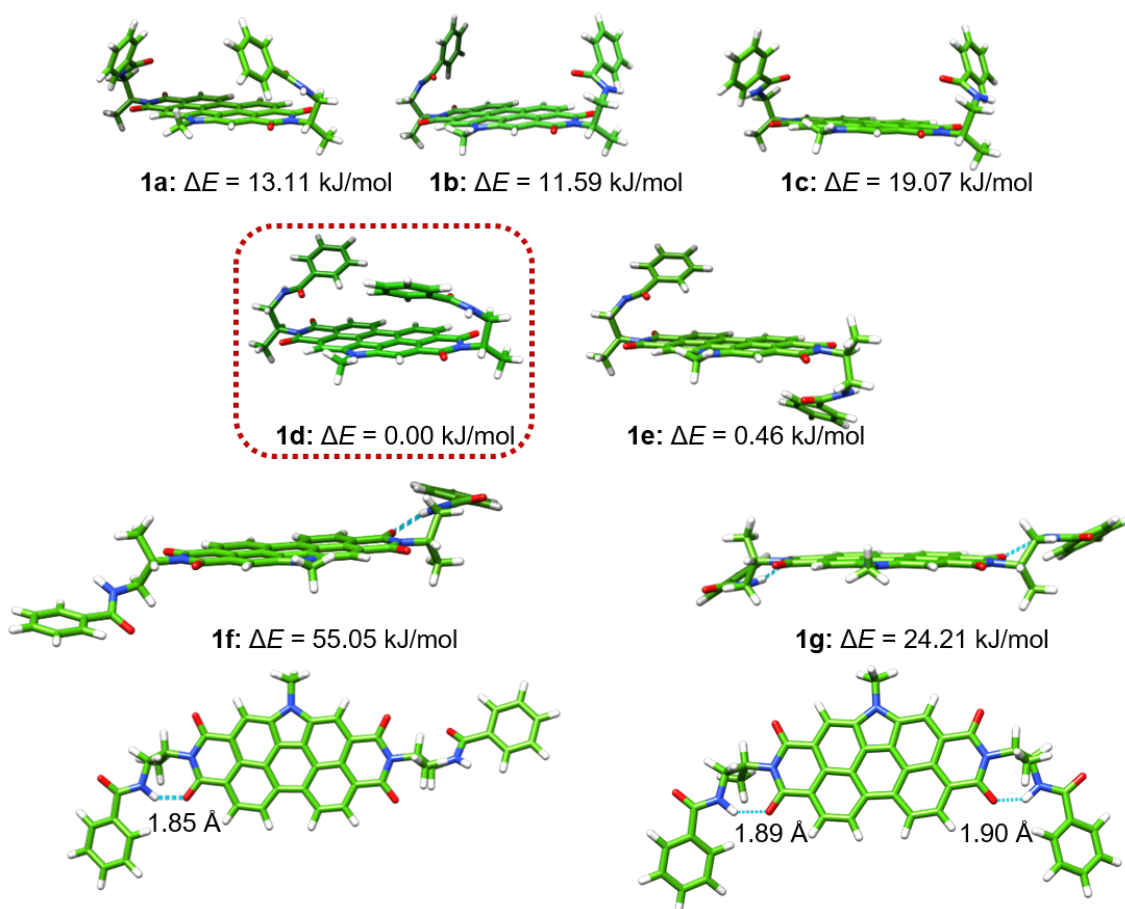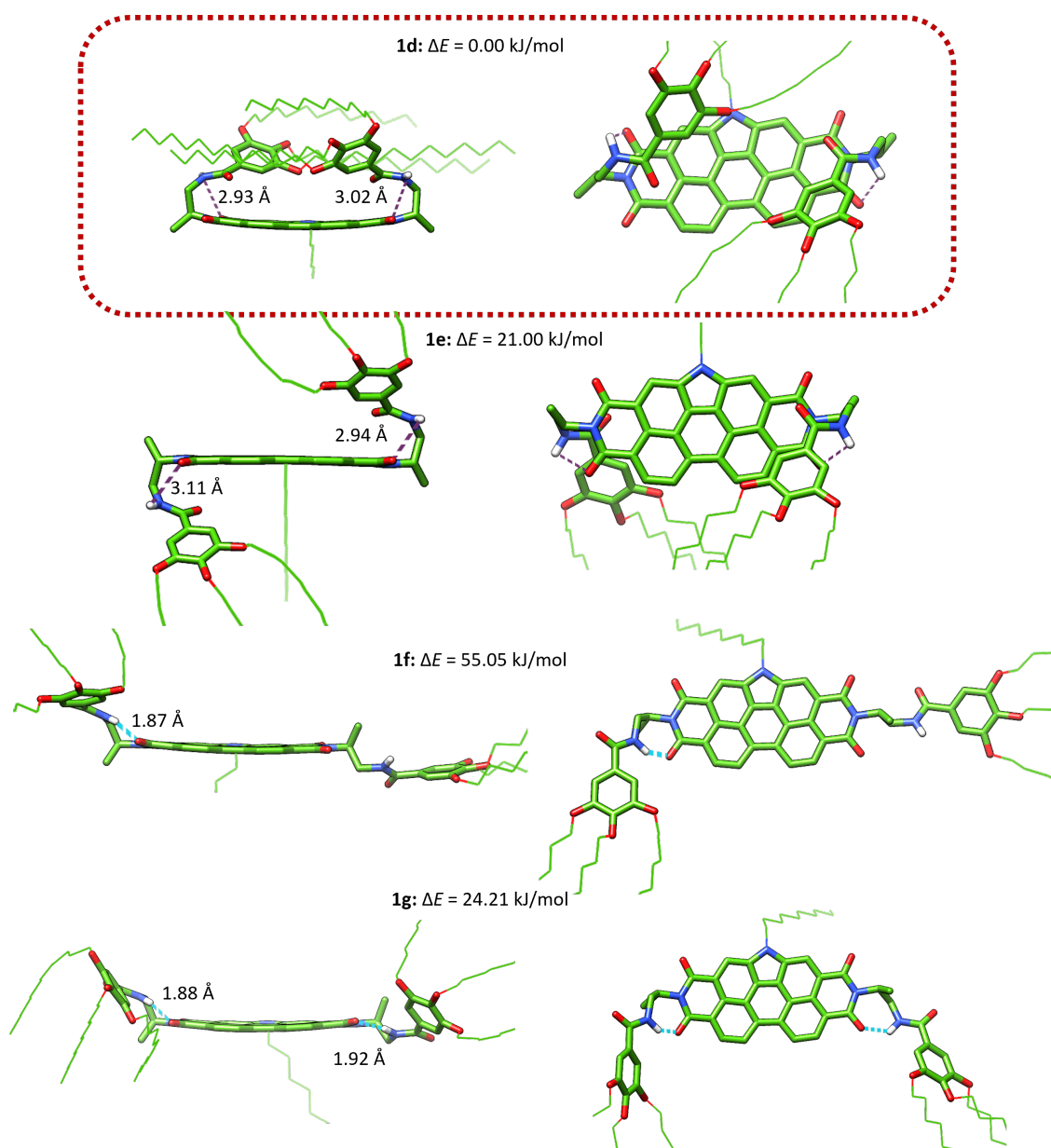**Figure S6**. Minimum-energy structures (with their relative energy indicated) computed at the GFN2-xTB level in CHCl$_3$ for the most stable conformers of monomer **1d**, **1e**, **1f**, and **1g** endowed with the peripheral side chains. Note that the terminal alkoxy chains have been cut in some cases for clarity purposes.

Figure S7. Side and top view of the minimum-energy structure computed at the GFN2-xTB level for dimer **D1d** endowed with the peripheral side chains. Its relative energy with respect to the most stable dimer (**D1d**) is indicated.
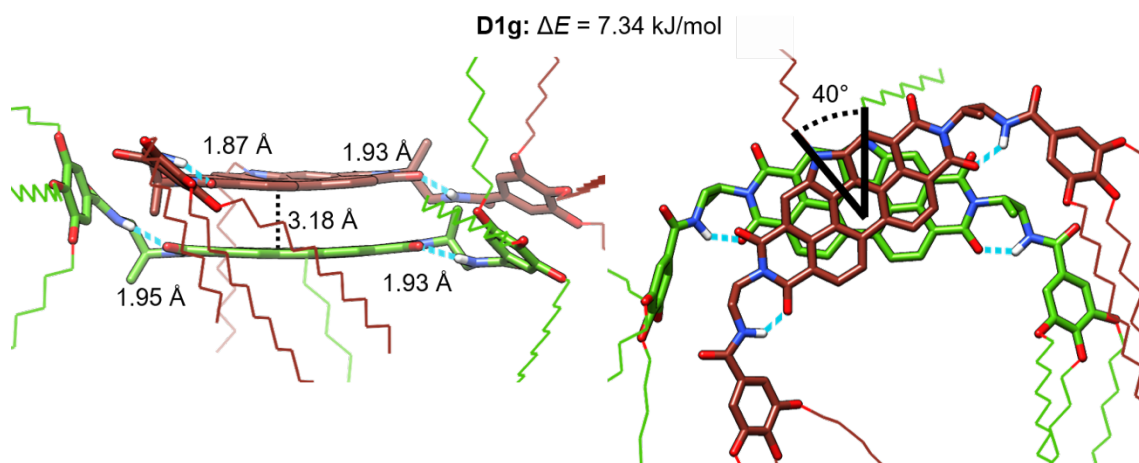
Figure S8. Side and top view of the minimum-energy structure computed at the GFN2-xTB level for dimer **D1g** endowed with the peripheral side chains. Its relative energy with respect to the most stable dimer (**D1d**) is indicated.

D1f: ΔE = 19.16 kJ/mol
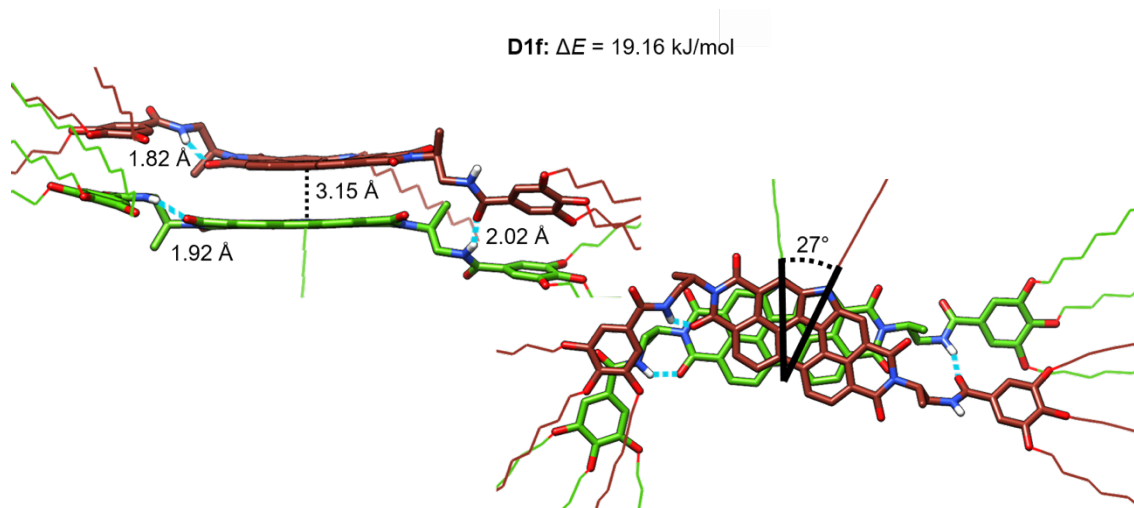
Figure S9. Side and top view of the minimum-energy structure computed at the GFN2-xTB level for dimer **D1f** endowed with the peripheral side chains. Its relative energy with respect to the most stable dimer (**D1d**) is indicated.
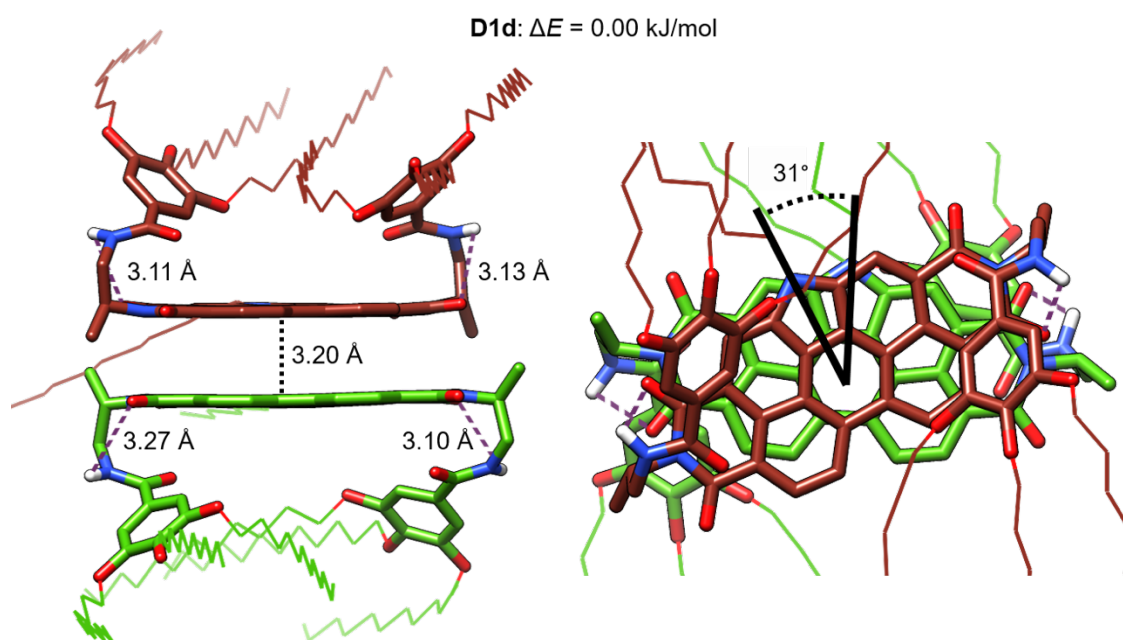
D1h: ΔE = 106.83 kJ/mol
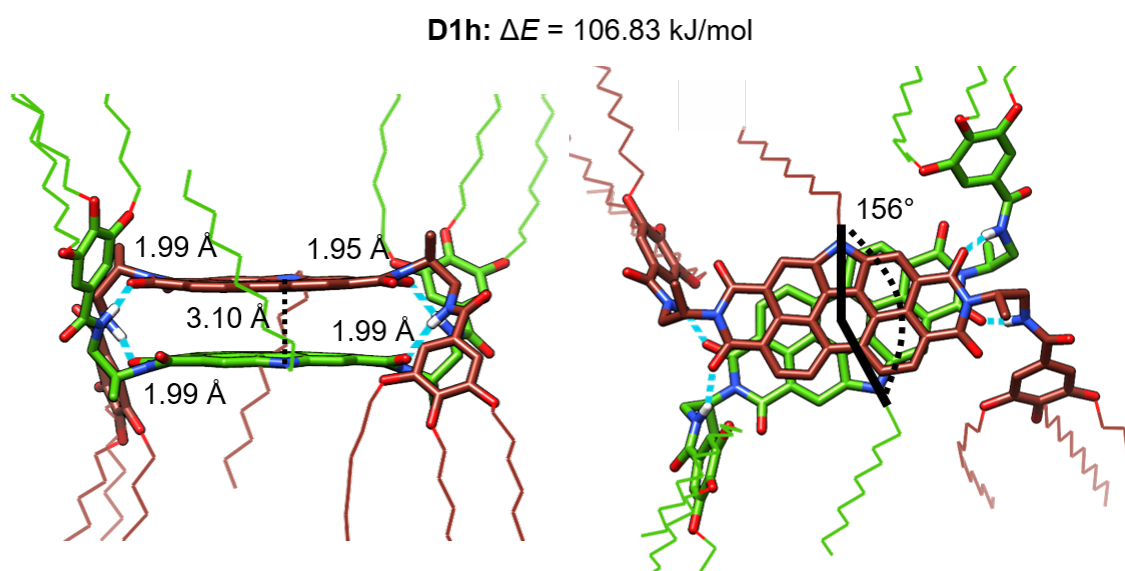
Figure S10. Side and top view of the minimum-energy structure computed at the GFN2-xTB level for dimer **D1h** endowed with the peripheral side chains. Its relative energy with respect to the most stable dimer (**D1d**) is indicated.
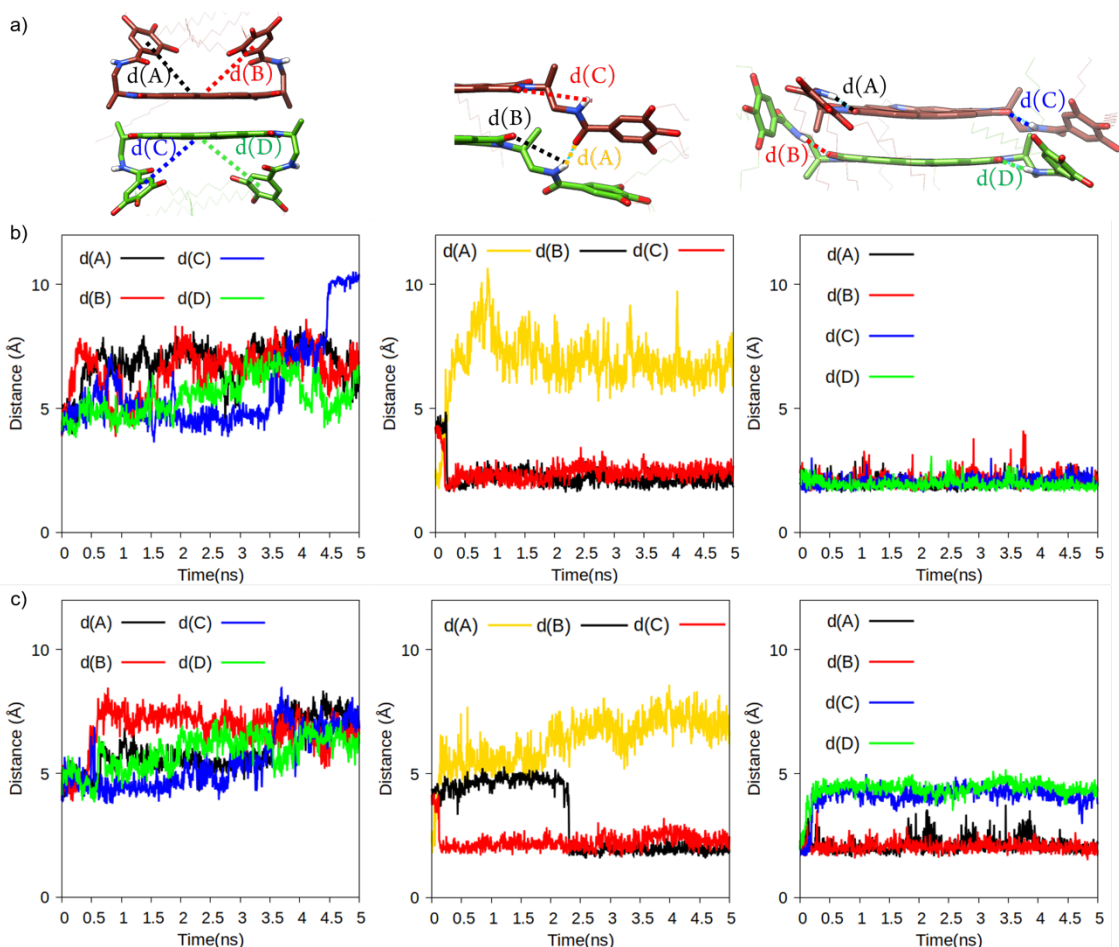
Figure S11. (a) Labeling of the relevant intra and intermolecular contacts to analyze the structural changes of dimers **D1d** (left), **D1f** (center)**,** and **D1g** (right) along the MD simulations. Evolution of the selected intra and intermolecular distances of dimers **D1d**, **D1f,** and **D1g** along the dynamics simulations in CHCl$_3$ (b) and MCH (c).
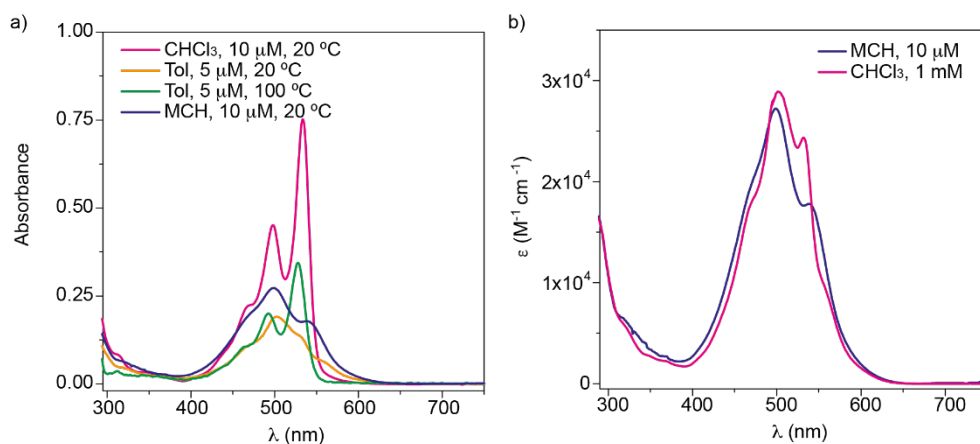
Figure S12. (a) UV-Vis spectra of **1** in different solvents. (b) UV-Vis spectra of **1** in MCH and CHCl$_3$ at c_T = 10 μM and 1 mM, respectively.
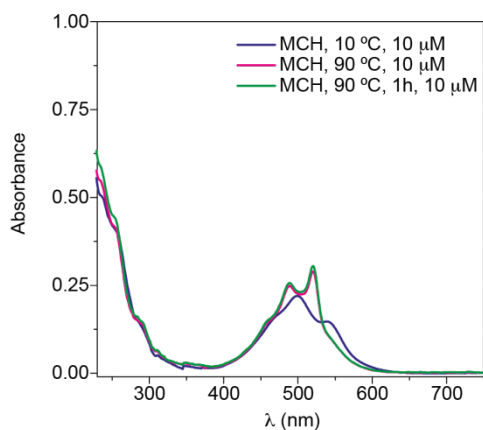
Figure S13. UV-Vis spectra of **1** in MCH at different temperatures ($c_T = 10\ \mu M$).
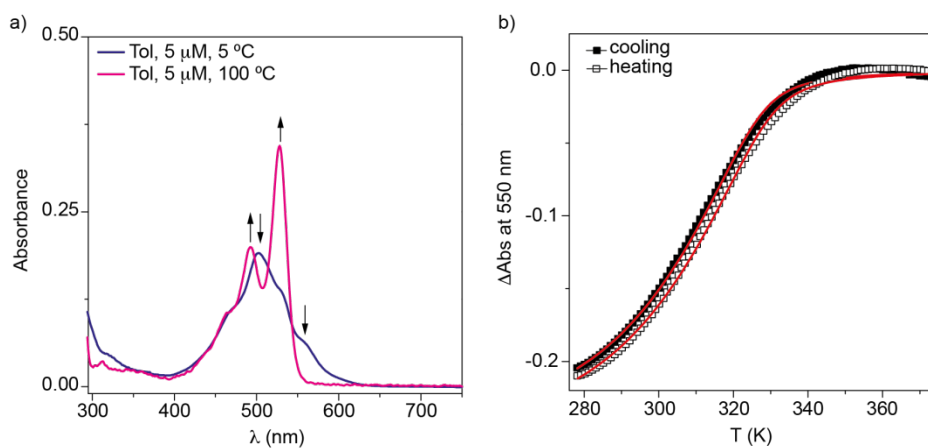
Figure S14. (a) UV-Vis spectra of **1** in Tol at $c_T = 5\ \mu M$. (b) Plot of the variation of the absorbance at 550 nm against temperature. The solid and hollow squares correspond to the cooling and heating processes at 1 K min^{-1}. The red lines in panel (b) depict the fitting to the one-component EQ model.
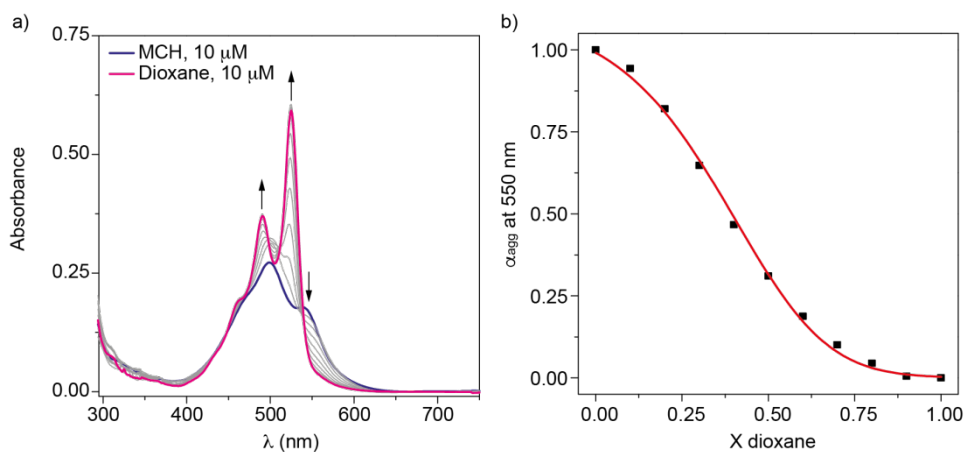
Figure S15. UV-Vis spectra (a) and denaturation curve (b) of **1** in MCH/dioxane mixtures (c_T = 10 μM). The red line in panel (b) depicts the fit to the SD model.
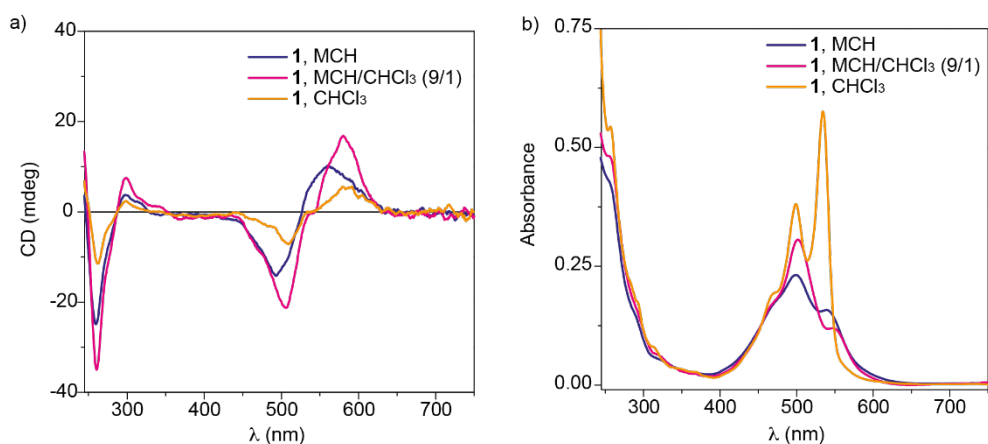
Figure S16. CD (a) and UV-Vis (b) spectra of **1** in MCH; MCH/CHCl$_3$ (9/1) mixture, and CHCl$_3$ (c_T = 10 μM, 10 ^{o}C).
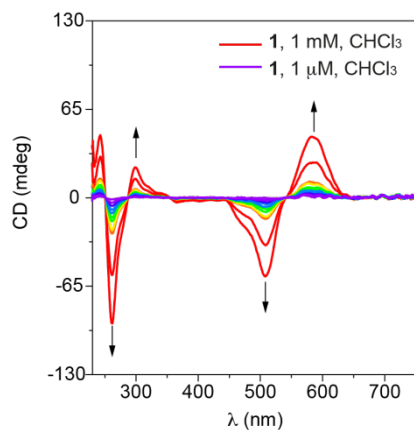
Figure S17. CD spectra of **1** in CHCl$_3$ at different concentrations.
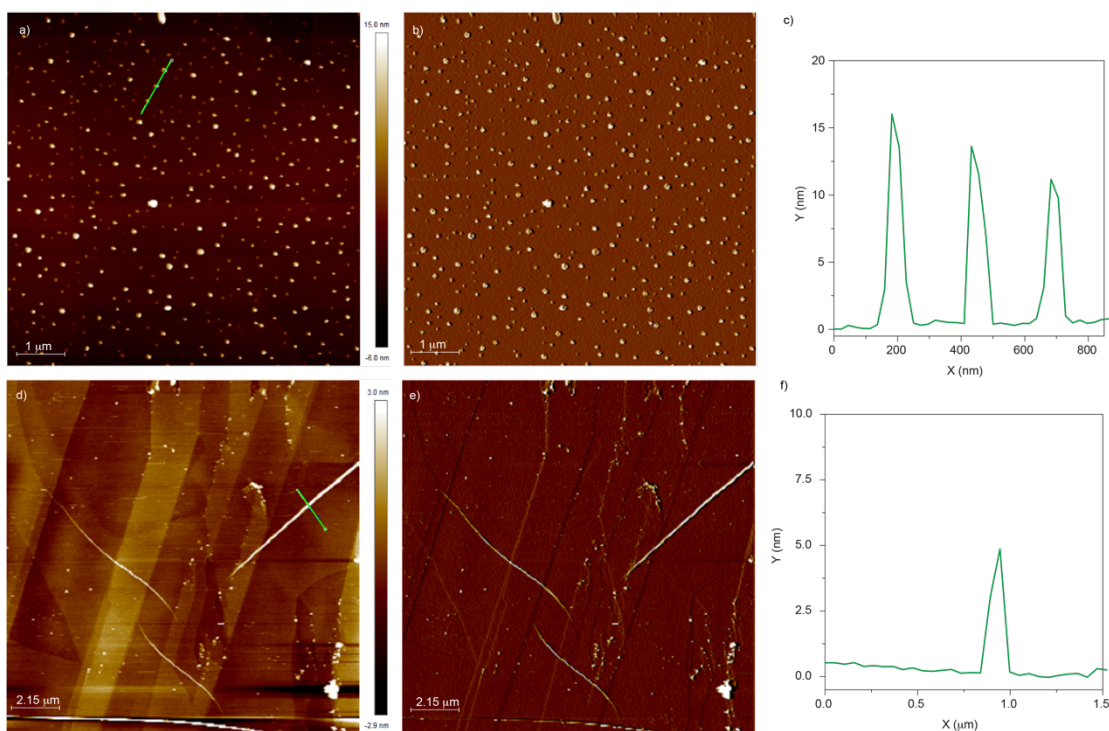
Figure S18. Height (a, d) and phase (b, e) AFM images of the nanoparticles (a, b) and isolated fibers (d, e) formed by **1**. (c, f) Height profile of the nanoparticles and isolated fibers along the green line in (a) and (d). Experimental conditions: HOPG as surface, $CHCl_3$ solvent in (a) and (b); MCH as solvent in (d) and (e); $c_T = 50$ and 10 μm for $CHCl_3$ and MCH, respectively.
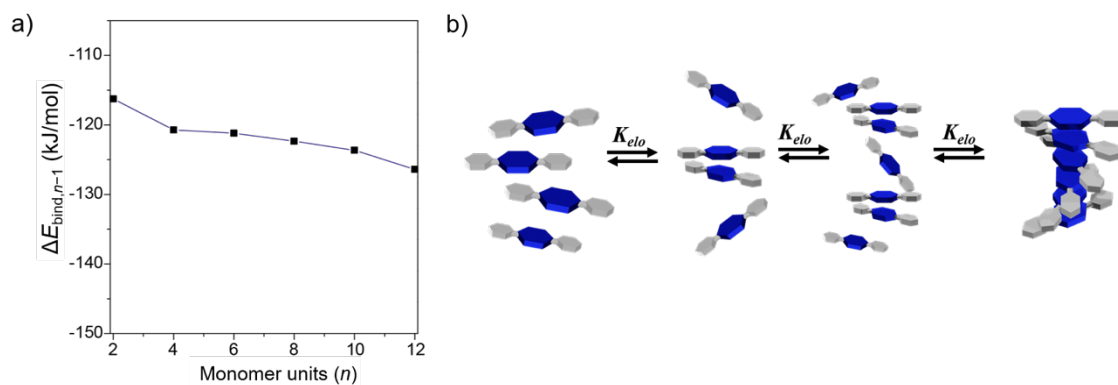
Figure S19. a) Stabilization energy per interacting pair ($\Delta E_{bind,n-1}$) as the number of monomers (n) in the (**1**)$_n$ aggregate increases. b) Schematic illustration of the isodesmic supramolecular polymerization of **1**.
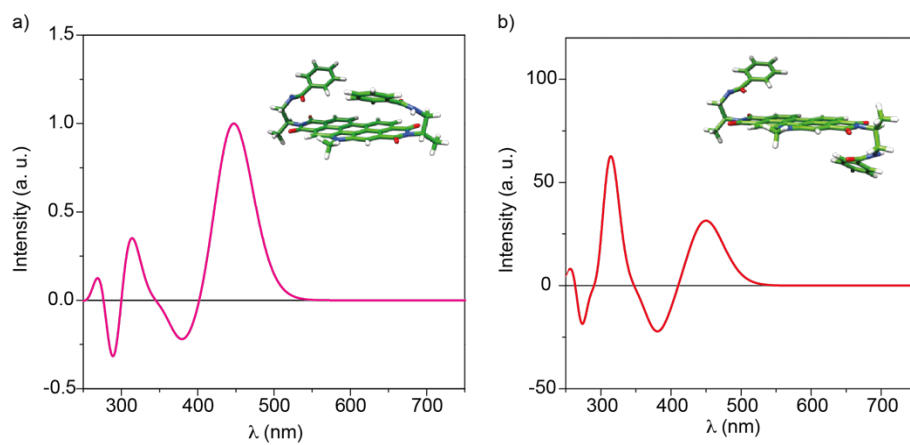
Figure S20. Simulated CD spectra calculated at the ωB97XD/6-31G** level for conformer **1d** (a) and **1e** (b).

5. Theoretical Details

The conformational space of a simplified monomeric unit of **1**, where peripheral dodecyloxy side chains are removed and the aliphatic $C_{10}H_{21}$ chain attached to the nitrogen atom of the NPBI core is substituted by a methyl group, was explored through the novel Conformer–Rotamer Ensemble Sampling Tool (CREST)[S3] using the xtb-6.1 program package including chloroform ($CHCl_3$) as solvent.[S4,S5] Solvent effects were included by means of the generalized Born surface area (GBSA) formulation. The main objective was to perform an extensive study of all possible conformers of a resulting from the flexible nature of the ethyl benzamide peripheral groups. Figure S5 displays the most stable conformers found for **1** after geometry optimization in $CHCl_3$ at the semiempirical GFN2-xTB[S5] level of theory as implemented in the xTB program. The GFN2-xTB method is based on a Hamiltonian similar to the well-known DFTB3, with a minimal valence basis set centered on atoms (STO-mG), and includes the density-dependent D4[S6] dispersion correction. Among the different conformers (Figure S5), the most stable structures are those with a *syn-* (**1d**, 0.00 kJ mol^{-1}) and *anti*-disposition (**1e**, 0.46 kJ mol^{-1}) of the outer benzamide groups over the NPBI core. Conformers **1f** and **1g**, in which the peripheral groups point outwards from the NPBI core, display a molecular geometry more suitable to promote the self-assembly (see below), although they are significantly higher in energy (55.05 and 24.21 kJ mol^{-1}, respectively). Both **1f** and **1g** have an *anti*-disposition of the peripheral groups with respect to the NPBI plane, but the difference orientation of the benzamide groups determines that only one of these groups forms a hydrogen bond with the adjacent imide group in conformer **1f**, whereas both benzamide groups form intramolecular hydrogen bonds in **1g** (distances of 1.90 Å).

In order to have a more realistic description of the structure an relative stability of the conformers of **1**, the most stable conformers (**1d** and **1e)** and those prone to promote the supramolecular self-assembly (**1f** and **1g**) were recalculated using the complete chemical structure of **1**; *i.e.,* after incorporating the dodecylalkoxy chains attached to the benzamide moieties and the decyl alkyl chain linked to the central nitrogen of the NPBI core. The minimum-energy geometry of each conformer (Figure S6) was obtained after full geometry relaxation at the GFN2-xTB level with $CHCl_3$ as solvent. A larger energy difference between these four conformers is now obtained. Conformer **1d** remains as the most stable and the energy difference with the other three conformers is increased. Conformers **1f** and **1g** preserve their favorable orientation for an optimal self-assembly and they considered together with **1d** to study the formation of possible dimers.

Conformer **1e** was discarded because the supramolecular growing is blocked by the arrangement of the peripheral side chains (Figure S6).

Dimers **D1d**, **D1f**, and **D1g** were built up from the respective **1d**, **1f**, and **1g** monomers and were fully optimized at the GFN2-xTB level in CHCl$_3$. Only a parallel arrangement of the NPBI cores, with the pyrrolic units pointing in the same direction, was considered in building up the dimers because it has been reported to be notably more stable than the antiparallel disposition.[S2,S7] The optimized dimers are close in energy, the maximum energy difference being of 19.16 kJ mol^{-1} between **D1d** and **D1f**, and present short π–π contacts between the NPBI cores (Figure 3b). Dimer **D1f** presents at one end an intermolecular N—H···O bond between the two monomers at 2.02 Å and, at the other end, two intramolecular N—H···O bonds with distances of 1.82 and 1.92 Å, respectively. In contrast, dimer **D1g** presents intramolecular H-bonds (1.92 Å) at both ends of the monomeric units. It should be noted that only the **D1f** and **D1g** dimers will be able to give rise to larger aggregates.

To disentangle the stability of the dimeric structures **D1d**, **D1f**, and **D1g**, and to elucidate the dimeric structure experimentally observed in CHCl$_3$ at high concentration, molecular dynamics (MD) simulations in CHCl$_3$ as solvent were performed with GROMACS 2021.3 using periodic boundary conditions.[S8] For N-PBI and CHCl$_3$ molecules, we used the OPLS-AA force field with atom type selection as assigned by the PolyParGen tool.[S9] Initial structures were those previously optimized at semiempirical level (GFN2-xTB) and point charges were calculated at the ωB97XD/6-31G** level[S10] within the Gaussian 16 A.03 program package.[S11] Prior to the molecular dynamic simulation of the different dimers, a suitable CHCl$_3$ solvent model was created. Briefly, an initial box containing 202 CHCl$_3$ molecules was built, minimized, equilibrated, and, subsequently, a MD simulation was performed. The computed density for the CHCl$_3$ box is 1.478 g mL^{-1}, which is close to the experimental density (1.489 g mL^{-1}). The good agreement achieved between theoretical and experimental densities indicates that the equilibrated box is representative of the chloroform solvent and, thus, can be safely used in the MD simulation of dimers.

A standard protocol was used for the MD simulations of the dimers: i) energy minimization of solute and solvent, ii) solvent equilibration around the solute, and iii) production. For energy minimization, we used a steepest descent algorithm with 0.01 nm step size until all forces were below 1000 kJ mol^{-1}·nm^{-1}. The equilibration of the solvent around the solute consisted of two stages of 2 ns in steps of 1 fs in which the solute was kept frozen: an initial NVT scheme fixing volume and temperature (283 K), and, subsequently, an NPT

scheme where pressure (1 bar) and temperature (283 K) were kept constant. Finally, the production run (NPT scheme) consisted of 5 ns calculations in steps of 1 fs. In all cases, we used a Vrescale thermostat with damping constant of 0.1 ps and a Parrinello-Rahman pressure coupling with damping constant of 2 ps. The cutoff radius for short-range electrostatic and van der Waals interactions was set to 1.0 nm and we used an order-4 particle mesh Ewald (PME) approach for long-range electrostatics.

Figure S11 shows the evolution of the most relevant intra and intermolecular contacts to analyze the structural changes taking place during the dynamics for dimers **D1d**, **D1f,** and **D1g**. For the **D1d** dimer, the outer benzamide groups evolve from their initial position covering the NPBI surface to a more extended disposition pointing away from the NPBI core in a similar arrangement to the **D1g** dimer. This can be seen by the steady increase of the distances between the centroids of the benzene rings of the benzoate groups and the centroid of the central benzene ring of the core (Figure 11). For dimer **D1f**, the intermolecular hydrogen bond between the two monomeric units is broken after the first ns, allowing the peripheral ethyl benzoate groups to change orientation to the NPBI core and the formation of two intramolecular hydrogen bonds per NPBI monomer, which is similar to the structure proposed for the dimer **D1g**. This is supported by the evolution of hydrogen bond distances in Figure S11b. In contrast, in the simulation of dimer **D1g**, the distances of four intramolecular hydrogen bonds barely change along dynamic simulation (Figure S11b). Therefore, dimer **D1d** and **D1f** evolve to a similar structure of **D1g** dimer. From the results obtained in the MD simulations, the dimeric structure registered experimentally at high concentrations of compound **1** in CHCl$_3$ corresponds to a similar structure to **D1g**. Dynamics of the **D1d, D1f** and **D1g** in MCH have also been carried out following the same protocol as the dynamics performed with chloroform. The obtained results in MCH are quite similar to obtained in CHCl$_3$.

Dimer **D1g** was then used to build up a supramolecular hexadecamer (16-mer) constituted by sixteen **1g** monomers stacked up in a helical arrangement. The minimum-energy structure of the 16-mer was calculated at the GFN2-xTB level in *n*-hexane (parametrized solvent similar in nature to methylcyclohexane) (Figure 6). In the optimized helical supramolecular polymer, adjacent NPBIs units are separated by an intermolecular distance of 3.40 Å and rotated *ca.* 40° along the growing axis. To shed light on the polymerization mechanism operating in the self-assembling process of NPBIs, single-point GFN2-xTB level calculations in *n*-hexane were performed for (**1**)$_n$ oligomers of increasing length ($n = 2 – 12$) extracted from the central part of the previously-optimized 16-mer to mitigate undesirable terminal effects due to the lack of periodic boundary

conditions. The binding energy per interacting molecular pair ($\Delta E_{\text{bind},n-1}$) was computed using the following equation

$$\Delta E_{\text{bind},n-1} = \frac{E_{\text{stack}} - n \cdot E_{\text{monomer}}}{n-1} \tag{1}$$

where E_{stack} is the total energy of the stacked (**1**)$_n$ aggregate bearing n monomeric units and E_{monomer} is the energy calculated for the monomer. Theoretical calculations reveal that $\Delta E_{\text{bind},n-1}$ barely changes with the oligomer size (Figure S19), which is indicative of an isodesmic supramolecular polymerization mechanism.

To understand the changes observed experimentally in the optical properties of compound **1** upon aggregation, a vibronic Hamiltonian similar in spirit to that proposed by F. Spano and co-workers was used to calculate the UV-Vis spectra of the aggregates[S12] (Figure 3). The vibronic Hamiltonian is the usual Frenkel exciton Hamiltonian

$$\hat{H} = \sum_{i,\tilde{v}} \left(E_i - \Delta + \tilde{v}\hbar\omega_{\text{eff}} \right) |i,\tilde{v}\rangle\langle i,\tilde{v}| + \sum_{i,j\neq i}\sum_{\tilde{v},\tilde{w}} J_{ij} \langle\tilde{v}|0\rangle\langle 0|\tilde{w}\rangle |i,\tilde{v}\rangle\langle j,\tilde{w}| \tag{2}$$

where $|i,\tilde{v}\rangle$ denotes a vibronic state in which monomer i is in its first electronic excited state (in its vibrational level $\tilde{v}$) and the other monomers are in their electronic and vibrational ground states. E_i is the excitation energy localized on molecule i, including zero-point energy corrections, and Δ is a solution-to-aggregate energy shift which accounts for nonresonant dispersion interactions between chromophores in the supramolecular assembly. $\hbar\omega_{\text{eff}}$ is the frequency of the effective intramolecular vibration (one per monomer). J_{ij} corresponds to the excitonic coupling between electronic states i and j, which is weighted by the Franck–Condon integrals (FCIs) $\langle\tilde{v}|0\rangle$ and $\langle 0|\tilde{w}\rangle$. FCIs within the displaced harmonic oscillator model depend on the Huang–Rhys (HR) factors between the involved electronic states.[S13] In our case, the HR factor between the ground state and the first electronic state S was used.

The eigenstates of the Hamiltonian in Eq. 2, for which cyclic boundary conditions were applied, can be described as a linear combination of the molecular excited states as:

$$|\psi_\alpha\rangle = \sum_{i,\tilde{v}} C_{i,\tilde{v}}^\alpha |i,\tilde{v}\rangle \tag{3}$$

where the $C_{i,\tilde{v}}^{\alpha}$ coefficients are obtained by diagonalization of the Hamiltonian. The maximum number of vibrational levels $\tilde{v}$ was set to be 5 because it provides a nice convergence of the calculated absorption spectra without compromising the size of the vibronic Hamiltonian. The homogeneous absorption spectrum $A(E)$ is derived from the sum over all eigenstates $|\psi_{\alpha}\rangle$ of the aggregate Hamiltonian as

$$A(E) = \sum_{\alpha} f_{\alpha} W_{LS}(E_{\alpha} - E) \qquad (4)$$

where the oscillator strengths f_{α} are evaluated as $f_{\alpha} = (2/3)E_{\alpha}\left|\langle\psi_{\alpha}|\hat{\mu}|G\rangle\right|^{2}$, E_{α} is the energy of the eigenstate $|\psi_{\alpha}\rangle$, $|G\rangle$ denotes the state where all the molecules are in their ground state, and $\hat{\mu}$ corresponds to the electric dipole moment operator. Finally, $W_{LS}(E_{\alpha} - E)$ represents a Gaussian shape function.

Table S1. Parameters (in eV) used in the vibronic Hamiltonian employed to calculate the UV-vis and CD spectra of the supramolecular D1g aggregates.

Parameters	eV
E_i	2.590
Δ	0.420
$\hbar\omega_{\text{eff}}$	0.161
J_{ij}	0.096
S	0.690[a]

[a]The HR factor is adimensional.

Table S1 gathers all the parameters used in the vibronic Hamiltonian. Most of these parameters were evaluated using data obtained from density functional theory (DFT) and time-dependent DFT (TD-DFT) calculations on monomer and dimer **D1g** using only the *N*-annulated PBI core within the Gaussian 16 A.03 program package. The E_i energy of the first bright electronic $S_0 \rightarrow S_1$ transition was estimated from the optimization of the monomer at the TDDFT level with the ωB97XD functional and the 6-31G** basis. The gas-phase energy was shifted to match the experimental values through the parameter Δ. The effective frequency $\hbar\omega_{\text{eff}}$ and the S factor were derived from the experimental absorption spectrum of compound **1** (monomer) according to Spano and co-workers.[S14] The intermolecular parameter (J_{ij}) was evaluated by using the optimized dimer **D1g**. TDDFT calculations were performed at the ωB97XD/6-31G** level in *n*-hexane to

estimate the intermolecular excitonic J_{ij} couplings by using the approximation developed by Curutchet and Mennucci (EET keyword in Gaussian).[S15]

Circular dichroism (CD) spectra calculated for dimer and decamer models (Figure 6) were also simulated by using the previous vibronic Hamiltonian with the parameters of Table S1. Rotational strengths for the vibronic states were calculated according to Loco and co-workers[S16] and implemented in our homemade code. The good agreement between the experimental CD spectrum and the one calculated for the aggregate allows us to verify that the NPBI derivative studied can self-assemble forming the proposed helical aggregate.

6. References

(S1) Wehner, M.; Röhr, M. I. S.; Bühler, M.; Stepanenko, V.; Wagner, W.; Würthner, F. *J. Am. Chem. Soc.* **2019**, *141*, 6092–6107.

(S2) Greciano, E. E.; Calbo, J.; Ortí, E.; Sánchez, L. *Angew. Chem. Int. Ed.* **2020**, *59*, 17517–17524.

(S3) Pracht, P.; Bohle, F.; Grimme, S. *Phys. Chem. Chem. Phys.* **2020**, *22*, 7169-7192.

(S4) Grimme, S.; Bannwarth, C.; Shushkov, P. *J. Chem. Theory Comput.* **2017**, *13*, 1989–2009.

(S5) Bannwarth, C.; Ehlert, S.; Grimme, S. *J. Chem. Theory Comput.* **2019**, *15*, 1652–1671.

(S6) Caldeweyher, E.; Bannwarth, C.; Grimme, S. *J. Chem. Phys.* **2017**, *147*, 034112.

(S7) Martínez, M. A.; Doncel-Giménez, A.; Cerdá, J.; Calbo, J.; Rodríguez, R.; Aragó, J.; Crassous, J.; Ortí, E.; Sánchez, L. *J. Am. Chem. Soc.* **2021**, *143*, 13281–13291

(S8) Abraham, M. J.; Murtola, T.; Schulz, R.; Pall, S.; Smith, J. C.; Hess, B.; Lindahl, E. *SoftwareX* **2015**, *1–2*, 19-25.

(S9) Yabe, M.; Mori, K.; Takeda, M. *J. Comput. Chem. Jpn Int. Ed.* **2019**, *5*, 2018-0034.

(S10) (a) Lee, C.; Yang, W.; Parr, R. G. *Phys. Rev. B.* **1988**, *37*, 785–789. (b) Becke, A. D. *J. Chem. Phys.* **1993**, *98*, 5648–5652.(c) Chai, D.; Head-Gordon, M. *Phys. Chem. Chem. Phys.* **2008**, *10*, 6615-6620. (d) Stein, T.; Kronik, L.; Baer, R. *J. Am. Chem. Soc.* **2009**, *131*, 2818-2820.(e) Francl, M. M.; Pietro, W. J.; Hehre, W. J.; Binkley, J. S.; Gordon, M. S.; Defrees, D. J.; Pople, J. A. *J. Chem. Phys.* **1982**, *77*, 3654–3665.

(S11) Gaussian 16, Revision A.03, Frisch, M. J.; Trucks, G. W.; Schlegel, H. B.; Scuseria, G. E.; Robb, M. A.; Cheeseman, J. R.; Scalmani, G.; Barone, V.; Petersson, G. A.; Nakatsuji, H.; Li, X.; Caricato, M.; Marenich, A. V.; Bloino, J.; Janesko, B. G.; Gomperts, R.; Mennucci, B.; Hratchian, H. P.; Ortiz, J. V.; Izmaylov, A. F.; Sonnenberg, J. L.; Williams-Young, D.; Ding, F.; Lipparini, F.; Egidi, F.; Goings, J.; Peng, B.; Petrone, A.; Henderson, T.; Ranasinghe, D.; Zakrzewski, V. G.; Gao, J.; Rega, N.; Zheng, G.; Liang, W.; Hada, M.; Ehara, M.; Toyota, K.; Fukuda, R.; Hasegawa, J.; Ishida, M.; Nakajima, T.; Honda, Y.; Kitao, O.; Nakai, H.; Vreven, T.; Throssell, K.; Montgomery, J. A., Jr.; Peralta, J. E.; Ogliaro, F.; Bearpark, M. J.; Heyd, J. J.; Brothers, E. N.; Kudin, K. N.; Staroverov, V. N.; Keith, T. A.; Kobayashi, R.; Normand, J.; Raghavachari, K.; Rendell, A. P.; Burant, J. C.; Iyengar, S. S.; Tomasi, J.; Cossi, M.; Millam, J. M.; Klene, M.; Adamo, C.; Cammi, R.; Ochterski, J. W.; Martin, R. L.; Morokuma, K.; Farkas, O.; Foresman, J. B.; Fox, D. J. Gaussian, Inc., Wallingford CT, **2016.**

(S12) Hestand, N. J.; Spano, F. C. *Chem. Rev.* **2018**, *118*, 7069-7163

(S13) May, V.; Kühn, O. Wiley-VCH Verlag GmbH & Co. KGaA: Weinheim, Germany, **2011**.

(S14) Hestand, N. J.; Spano, F. C. *Chem. Rev.* **2018**, *118*, 7069-7163.

(S15) Curutchet, C.; Mennucci, B. *J. Am. Chem. Soc.* **2005**, *127*, 16733-16744

(S16) Loco, D.; Jurinovich, S.; Bari, L. Di; Mennucci, B. *Phys. Chem. Chem. Phys.* **2015**, *18*, 866–877.